Check for updates

Advanced Optical Materials

ADVANCED OPTICAL MATERIALS
www.advopticalmat.de

RESEARCH ARTICLE OPEN ACCESS

Incorporating Si into Sb_2Se_3: Tailoring Optical Phase Change Materials via Nanocomposites

Chih-Yu Lee[1] | Yi-Siou Huang[1,2] | Felix Adams[1] | Chuanyu Lian[1,2] | Hongyi Sun[1,2] | Jie Zhao[3] | Zichao Ye[3] | Nathan Youngblood[4] | Juejun Hu[5] | Leslie H Allen[3] | Yifei Mo[1] | Ichiro Takeuchi[1,6] | Carlos A Ríos Ocampo[1,2]

[1]Department of Materials Science and Engineering, College Park, University of Maryland, Maryland, USA | [2]Institute of Research in Electronics and Applied Physics, College Park, University of Maryland, Maryland, USA | [3]Department of Materials Science and Engineering, University of Illinois at Urbana-Champaign, Urbana, Illinois, USA | [4]Electrical and Computer Engineering Department, The University of Pittsburgh, Pittsburgh, Pennsylvania, USA | [5]Department of Materials Science & Engineering, MIT, Cambridge, Massachusetts, USA | [6]Maryland Quantum Materials Center, College Park, University of Maryland, Maryland, USA

Correspondence: Ichiro Takeuchi (takeuchi@umd.edu) | Carlos A Ríos Ocampo (riosc@umd.edu)

Received: 17 October 2025 | **Revised:** 22 December 2025 | **Accepted:** 25 January 2026

Keywords: chalcogenides | nano calorimetry | nanocomposites | optical materials | phase change materials | photonic integrated circuits

ABSTRACT

Optical phase change materials (OPCMs) have attracted attention for their versatility as nonvolatile photonic modulators. Discovering novel materials or engineering existing ones is therefore crucial to achieving the performance that current materials lack. Here, we employ co-sputtering to investigate the doping of Si into Sb_2Se_3. We investigate the optical, structural, and thermal properties and compare results with those obtained from first-principles calculations. We also study the crystallization and melt-quenching via nano-differential scanning calorimetry (NanoDSC). We find that 20% Si increases the transparency window in both states, specifically to 800 nm in the amorphous phase, while reducing power consumption by lowering the melting temperature—at the cost of reducing the refractive index contrast and slowing the kinetics of the phase transition. Moreover, we demonstrate switching between the amorphous and crystalline states of Si-Sb_2Se_3 using electro-thermal switching in photonic integrated devices, ~100-μm^2 microheaters, and the NanoDSC sensor. Importantly, we observe that phase segregation in recrystallized films forms a nanocomposite with Sb_2Se_3 grains in an amorphous matrix, allowing both reversible switching and effective-medium optical properties. By harnessing phase segregation rather than avoiding it, nanocomposites transform a potential failure mechanism into a design strategy, enabling deliberate tuning of OPCM properties through targeted dopant selection.

1 | Introduction

Chalcogenide-based optical phase change materials (OPCMs) have garnered attention in a wide range of applications, including photonic circuits [1–3], structural color [4], optical metamaterials [5–7], polariton nanophotonics [8], and others [9]. These applications leverage OPCM's nonvolatile optical responses and exploit the contrast in their refractive index and extinction coefficient. Finding novel OPCMs with a large refractive index, vanishing extinction coefficient, low power consumption, transparency window spanning into the visible spectrum, and high switching speed has therefore become essential for advancing these emerging fields [10].

Low-loss, wide-bandgap OPCMs can be engineered by introducing light chalcogens into conventional Te-based phase change materials (PCMs). The elemental substitution of tellurium with selenium in $Ge_2Sb_2Te_5$, for instance, significantly increases their optical bandgap, from 0.62 ($Ge_2Sb_2Te_5$) to 1.64 eV ($Ge_2Sb_2Se_5$). Hence, controlling the Se/Te content in the alloys enables

This is an open access article under the terms of the Creative Commons Attribution License, which permits use, distribution and reproduction in any medium, provided the original work is properly cited.

© 2026 The Author(s). *Advanced Optical Materials* published by Wiley-VCH GmbH

tailoring the materials' optical properties [11]. $Ge_2Sb_2Se_4Te_1$ [12], an intermediate alloy in the Te substitution with Se, is a well-known example of an OPCM with optimized properties, combining broadband transparency (1–18.5μm in the amorphous and ~2.4–18.5 μm in the crystalline state), large optical contrast (contrast in refractive index, $\Delta n = 1.5$), and improved thermal stability (crystallization temperature, T_c~300°C). As for binary compounds, Sb_2Se_3, previously studied in solar cell absorbers [13] and highly sensitive photodetectors [14], has become a popular OPCM for pure phase modulation in the telecommunication C-band (1550 nm), since it exhibits vanishing losses ($k < 10^{-5}$) in both the amorphous and crystalline states [15]. Sb_2Se_3 undergoes congruent melting, making it a robust material with demonstrated millions of switching cycles [16, 17]. While Sb_2Se_3 features an absorption edge close to ~900 nm, another OPCM, Sb_2S_3, stands out with even wider transparency down to ~600 nm in the amorphous state. Both Sb_2Se_3 and Sb_2S_3 are promising candidates for photonic applications; however, Sb_2Se_3 achieves an optimal balance between thermal stability and optical contrast and has proven to be more chemically inert and durable [15]. Sb_2Se_3, however, could benefit from further materials engineering to enhance its amorphous stability (T_c ~ 200°C) and transparency in the visible range—crucial for dielectric metasurfaces [18], quantum photonic platforms operating with visible or red–near-IR photons [19], and optical coatings [20].

While OPCMs can be tailored via modulating the number of electrons shared between adjacent atoms, i.e., chemical bonding [21], discovering new OPCMs using first-principles has proved difficult, particularly in the amorphous state [22]. Instead, incorporating dopants into a matrix of existing OPCMs via combinatorial deposition is a faster route to obtaining optimal materials, following a strategy that has been exploited widely in electrical phase change materials. For example, N [23], O [24], and C [25] are exploited as dielectric dopants, and Sc [26], Mn [27], and Cr [28] are considered as metal dopants to PCMs. In some previous studies, doping increases crystallization temperature and resistivity in amorphous and/or crystalline states, such as N-doped $Ge_2Sb_2Se_5$ [23] and O-doped Sb [29], due to the increased number of scattering sites and grain boundaries. Other examples include doping SiO_2 into an Sb matrix to create a nanocomposite with enhanced thermal properties [30] and doping metal oxides into Sb [31]. In both cases, Sb undergoes a phase transition, while the oxides act as a 3D confinement for adjacent regions.

Previous studies on doped Sb_2Se_3 focus on photovoltaic solar cells, such as Sn-doped Sb_2Se_3 [32] and Cu-doped Sb_2Se_3 [33]. Hu et al. showed Si-doped Sb_2Se (not Sb_2Se_3) as a promising PCM because of its higher crystallization temperature, larger crystallization activation energy, and better data retention ability [34]. Liu et al. demonstrated Si-doped Sb for higher stability in ultrafast operation [35]. However, there is a paucity of studies on the effects of dopants on the optical properties of OPCMs—specifically, their refractive index and extinction coefficient, as well as their phase change behavior. Here, we employ combinatorial and co-sputtering methods, shown in Figure 1a, to systematically investigate the effects of 0–20% Si doping in Sb_2Se_3 thin films and provide optical, structural, and thermal characterization data. We also perform Density Functional Theory (DFT) calculations on Si-doped Sb_2Se_3. We investigate the thermodynamics of Si-doped Sb_2Se_3 materials using ultrafast nano-differential scanning calorimetry (NanoDSC), which directly measures the quantitative thermal metrics (temperature, enthalpy, and heat capacity) by cycling OPCMs between amorphous and crystalline states. To further demonstrate reversible switching, we integrate Si-doped Sb_2Se_3 into photonic integrated circuits (PICs) with embedded microheaters for electro-thermal dynamic switching. By measuring the phase shifts upon OPCM switching, the PIC enables, in addition, measuring the OPCM's optical properties. Lastly, we performed reflectance measurements directly on the binary compound $SiSe_2$ - Sb_2Se_3, deposited on large microheaters.

2 | Materials Characterization

We start by characterizing thin films with binary composition spreads from Si and Sb_2Se_3 targets on 400 μm-thick, 3-inch sapphire wafers using an ultrahigh-vacuum (base pressure: 2×10^{-8} Torr) magnetron sputtering system. We deposited both continuous gradients and 3.5 × 3.5 mm^2 pads (see Figure 1a) by using a Si mask and proceeded to perform optical, structural, and thermal characterization. See Experimental Section for more details about sample preparation.

2.1 | Optical Properties

We used the Tauc-Lorentz model to fit the complex refractive index of the different compositions and derive the optical bandgaps from the dispersion model, as shown in Figure 1b–d. The refractive index (n), extinction coefficient (k), and bandgap (E_g) of pure Sb_2Se_3 are comparable to those reported in literature [36, 37]. Note that optical constants vary slightly across different synthesis methods owing to variations in film morphology, roughness, density, and microstructure. Hence, we considered undoped Sb_2Se_3 as the baseline for all comparisons. We prepared Si and Sb_2Se_3 compositional combinations in both patterned spreads and in continuous spreads to avoid edge-related artifacts in the ellipsometry characterization (see Figures S1 and S2). For the as-deposited amorphous film, the E_g changes from 1.37 to 1.50 eV as the Si concentration increases from 0% to 20%, as shown in Figure 1b. The E_g first reduces slightly as Si reaches 1.5% and remains at ~1.30 eV until Si attains 13.4%. However, the bandgap climbs drastically after Si doping exceeds 15%. We note that the error margin of dispersive model fitting based on Tauc-Lorentz dispersion oscillators ranges from 0.002 to 0.008 eV; therefore, the bandgap fitting is considered reliable. The bandgap narrowing at low doping concentration can be attributed to band renormalization with impurities or band tailing, which is often observed as Urbach tailing [38, 39]. Figure 1c shows the refractive indices as a function of wavelength. While the absorption edge expands to 828 nm as Si increases, the value of n decreases. This is expected given Kramers-Kronig relations, with high n associated with low E_g, influenced also by several factors, such as electronic structure, phonon interaction, and band structure, that affect the relationship between them [40, 41]. Given that the phase transition temperature for each composition was unknown, we prepared samples annealed at 200°C, 240°C, and 350°C, respectively. We see, in Figure 1b, that the E_g of most compositions drops to 1.1 eV after 200°C annealing for over 20 min, which may indicate that the materials are fully crystallized. However, compositions with high Si% (>10%) required a higher

21951071, 2026, 8, Downloaded from https://advanced.onlinelibrary.wiley.com/doi/10.1002/adom.202503389, Wiley Online Library on [04/03/2026]. See the Terms and Conditions (https://onlinelibrary.wiley.com/terms-and-conditions) on Wiley Online Library for rules of use; OA articles are governed by the applicable Creative Commons License

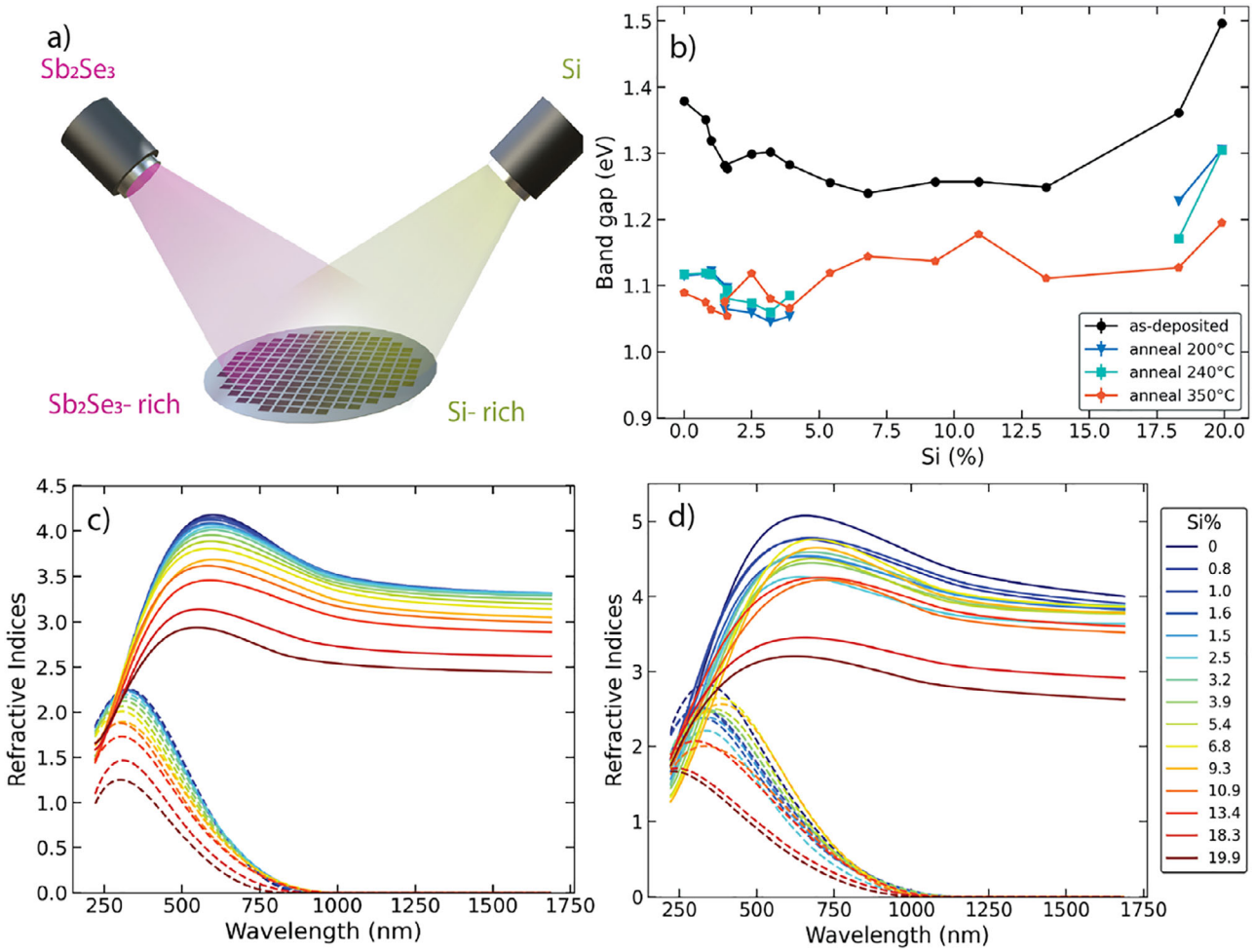

FIGURE 1 | Bandgap and refractive index characterization. (a) Schematic of co-sputtering. (b) Optical bandgap extracted from the ellipsometry measurement. The data were collected from different spreads (as deposited, annealed at 200°C, 240°C, and 350°C) across 15 compositions. (c) and (d) are wavelength-dependent refractive indices of different compositions measured as deposited and 350°C annealed, respectively. The solid lines correspond to the refractive index (n) and dashed lines to the extinction coefficient (k).

temperature to achieve a stable E_g, which for 20% Si decreases to ~1.2 eV after annealing at 350°C. The missing data points for 200°C and 240°C annealed samples exhibited abnormally low E_g values due to unreliable fitting arising from the edge effect in patterned spreads. The associated refractive indices are plotted in Figure 1d. Despite displaying a larger bandgap and contrast in optical properties, the crystallization of thin films proved challenging for higher Si compositions, which triggered our study on their phase transformations and associated thermodynamics/kinetics.

2.2 | Density Functional Theory (DFT) Calculations

We performed DFT calculations to investigate the effect of Si doping in crystalline Sb_2Se_3 from first principles. The computational models are based on single-phase Sb_2Se_3 with Si and vacancies on Sb sites, resulting in different compositions but similar Si concentrations as observed in our experiments (Figure 2a)—see the Experimental Section for more details on the doping mechanism and Figure S3 for the crystal structures. Figure 2b shows the DFT predicted bandgap as a function of Si concentration, which resembles the experimental results in Figure 1b, but the predicted bandgaps are lower, which could be attributed to a well-known systematic error in DFT calculations [42]. While there is no significant change in the bandgap at low Si concentrations, the bandgap increases by about 30% at the highest concentration calculated (15.8 at%). We note that these calculations assume that the material remains in a single phase, i.e., no crystal phase segregation. Subsequent experimental results suggest phase segregation into one crystalline phase and another Si-rich glassy phase. These DFT calculations, therefore, reflect the behavior of only the pre-segregation crystalline phase.

2.3 | X-ray Diffraction (XRD)

We measured temperature-dependent XRD on two samples: pure Sb_2Se_3 and 20% Si-doped Sb_2Se_3 to obtain structural information on as-deposited, crystalline, molten, and recrystallized states. In Figure 3a, the diffraction peaks for pure Sb_2Se_3 appear at 200°C and disappear after 600°C, which is consistent with the crystallization and melting temperatures, T_c and T_m, reported

21951071, 2026, 8, Downloaded from https://advanced.onlinelibrary.wiley.com/doi/10.1002/adom.202503389, Wiley Online Library on [04/03/2026]. See the Terms and Conditions (https://onlinelibrary.wiley.com/terms-and-conditions) on Wiley Online Library for rules of use; OA articles are governed by the applicable Creative Commons License

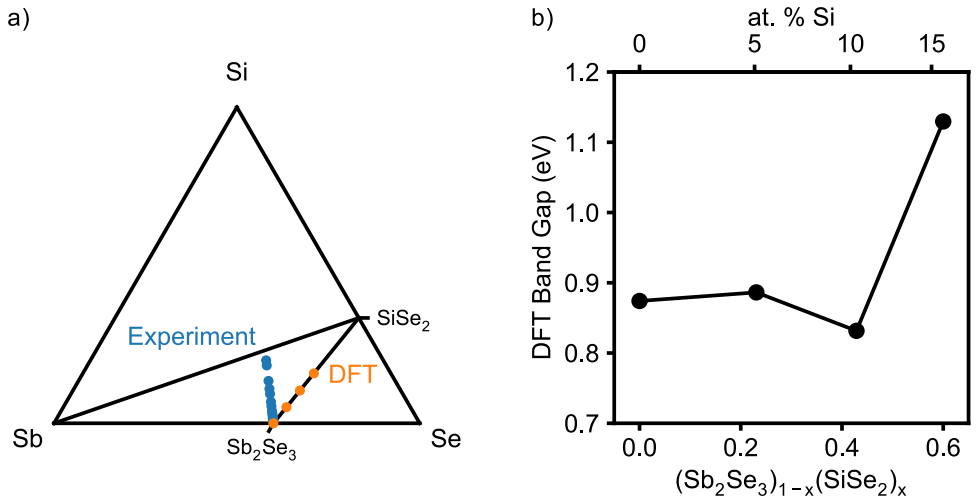

FIGURE 2 | The effects of Si substitution into Sb_2Se_3 as predicted by DFT. (a) The composition of the DFT supercells compared to the experimentally measured compositions. (b) The bandgap predicted by DFT as a function of Si concentration. The crystal structures are shown in Figure S3.

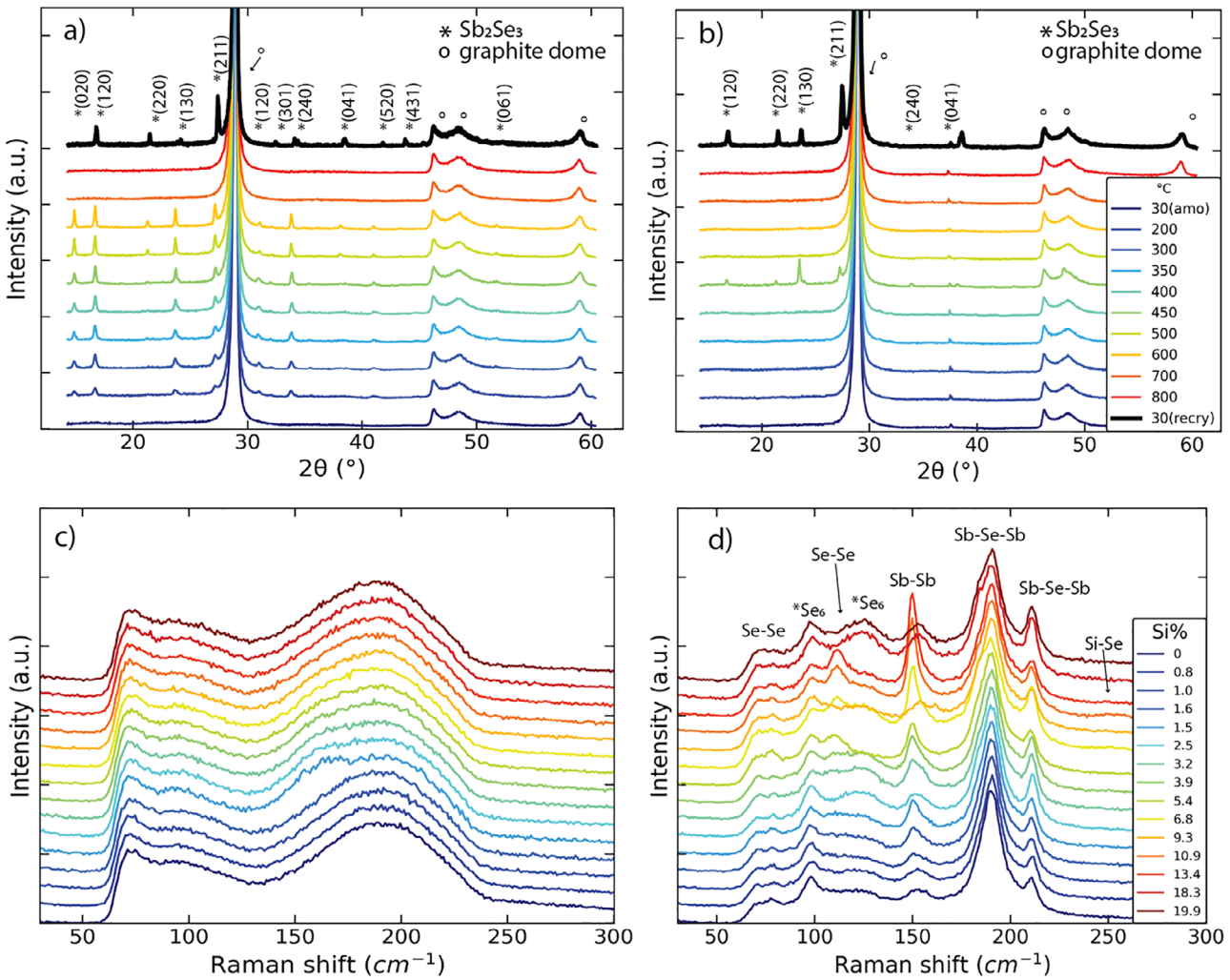

FIGURE 3 | Temperature-dependent XRD and composition- dependent Raman spectroscopy. (a) Sb_2Se_3 and (b) 20% Si-doped Sb_2Se_3 from 30°C amorphous (amo) to 800°C, and then quench down to room temperature, 30°C (recry). Raman spectroscopy for 15 compositions measured (c) as-deposited and (d) after 400°C annealing for over 20 min.

21951071, 2026, 8, Downloaded from https://advanced.onlinelibrary.wiley.com/doi/10.1002/adom.202503389, Wiley Online Library on [04/03/2026]. See the Terms and Conditions (https://onlinelibrary.wiley.com/terms-and-conditions) on Wiley Online Library for rules of use; OA articles are governed by the applicable Creative Commons License

in the literature [43]. The XRD patterns are identified as orthorhombic Sb_2Se_3, again matching previous studies. Figure 3b demonstrates that 20% Si-doped Sb_2Se_3 crystallizes at 400°C, and surprisingly, it melts at 500°C, indicating a relatively narrow operational window for achieving crystallization on a device. The preferred orientations are also slightly different from pure Sb_2Se_3. For example, the (020) and (120) orientations are not obvious, whereas the (130) orientation is preferred; no additional peaks were observed. Despite exhibiting a smaller grain size and a potential reduced degree of crystallinity, as inferred from the Scherrer analysis (see Figure S4), the doped sample retains a long-range crystal structure similar to that of pristine Sb_2Se_3. They both exhibit a shift toward higher 2θ in recrystallization compared to the first crystallization, which might indicate the compressive force applied on the films by the capping layer while the crystal grows. We do not observe a second phase with a different crystal structure. The temperature-dependent XRD results align well with those of the hot-plate annealed samples in Figure 1, in that Si-doped samples are more challenging to crystallize. With these results, we confirm that Si dopants suppress the crystallization of amorphous films, similar to previously reported results for Si-doped Sb_2Te_3 [45].

2.4 | Raman Spectroscopy

We employed Raman spectroscopy to probe the bonding interactions in the short-range order. This technique also enables us to monitor changes in bonding characteristics following the annealing process across various Si concentrations. In Figure 3c, all compositions of as-deposited Si-doped Sb_2Se_3 demonstrate a similar Raman spectrum, exhibiting a prominent broad peak centered at approximately 190 cm^{-1}, which corresponds to the characteristic signature of amorphous Sb_2Se_3 [15]. No Si-Si peak ~500 cm^{-1} was observed in any of the samples, which is why we focus on analyzing Raman signatures below 300 cm^{-1}. Following the annealing process at 400°C for 20 min on a hotplate, the previously observed broad peak near 190 cm^{-1} resolved into two distinct, sharper peaks at approximately 190 and 210 cm^{-1}. This transition indicates an increase in Sb_2Se_3 crystallinity. The resulting peaks are attributed to the Sb−Se−Sb bending vibrations characteristic of the Sb_2Se_3 orthorhombic structure [13, 44]. Additional Raman peaks are observed after the annealing process. The peaks at 110 and 150 cm^{-1} indicate the presence of Sb-Sb bonding [46, 47]. The peaks around 100 and 130 cm^{-1} are attributed to the Se_6 rhombohedral ring structure, while the features near 80 cm^{-1} are linked to Se-Se bonding contributions. Notably, the Raman peak observed at around 250 cm^{-1} appears in the sample regions with relatively high silicon concentrations and lower Sb_2Se_3 concentrations. Therefore, we propose that this peak most likely originates from Si-Se interactions, which we observe more clearly later in Section 3 [47, 48]. It is noticeable that the Si-Se resonance bond appears at 6.8% and 10.9% of Si doping, which implies the potential substitution of Si into Sb sites, consistent with DFT calculations, suggesting the formation of $SiSe_2$, the stable Si-Se glass at ambient conditions [49, 50]. This resonance becomes negligible in the highly Si-doped region (>10%), likely due to disorder (i.e., the sample did not fully crystallize after this annealing), indicating that potential Si-Se bonds are still absent.

2.5 | Nanocalorimetry and TEM

Nano-differential scanning calorimetry, or NanoDSC [51–53], is a technique that uses a microscale device for thin-film DSC characterization, meeting industry standards with a sensitivity of 1 Å and a scanning rate up to 3×10^6 K/s. In addition to thermal characterization, we utilize the NanoDSC device to cycle the OPCMs reversibly, simulating a real OPCM device, which alleviates concerns about the transferability of results from characterization systems to their practical application.

To further investigate the thermodynamic effects of Si doping on the phase transition, we use co-sputtering on NanoDSC devices, as shown in Figure 4a,b. In Figure 4c, the $C_p(T)$ of the pre-scanned (the as-deposited sample melted by a scan to 650°C) 10% Si-doped sample shows a reproducible crystallization-melt similar to the undoped sample, with a T_c roughly 10 °C higher. From the kinetic study in Figure 4e, we find that the activation energy of 10% Si-doped materials is lower (0.9 eV) than that of undoped materials (1.2 eV). This activation energy is derived from the Kissinger analysis of the crystallization curve, as described in our prior work [54]. However, the first $C_p(T)$ scan of the as-deposited 20% Si-doped sample, in Figure 4d, shows a significantly reduced melting temperature (T_m = 490 °C), which is 120 °C lower than that of pure Sb_2Se_3. These results agree with our XRD findings (crystalline peaks disappear at lower temperatures in Figure 3b) and the lower switching power observed in PIC platforms (see Section 3.1). Additionally, both the melting and crystallization enthalpy ($C_p(T)$ peak integral area) are much shallower than in undoped Sb_2Se_3, indicating that only part of the film undergoes the first crystallization-melting-quench cycle while the rest remains amorphous.

For TEM characterization, we applied electrical annealing (calorimetric pulses to 450 °C with a heating rate of 120,000 K/s) to the 20% Si-doped sample after the first melt-quench cycle to maximize its crystallinity, mimicking crystallization pulses in a real device (see Figure 4f). TEM reveals two phases, (g) glassy and (h) polycrystalline, in the recrystallized films. This indicates phase segregation after the first cycle. The (g) phase shows minor dewetting with irregular morphology, and diffusion rings are observed in TEM diffraction patterns (Figure 4g: 1). The other phase has a more defined round shape, confirmed as grains with different orientations (Figure 4g: 2–4). Since the phase is amorphous, there are no crystalline peaks in the XRD patterns of the recrystallized 20% Si-doped sample, as shown in Figure 3b. The segregated nanocomposite exhibits an average grain size of ~270 nm, with a range of 70–500 nm (see Figure S5). We hypothesize that the (g) phase is associated with Si-rich composition and the formation of $SiSe_2$, supported by a qualitative EDS study, shown in Figure S6. However, due to the complexity of the multi-layered device structure and nanoscale features, it was challenging to accurately probe nanocomposites and to quantitatively isolate Si from the background (SiN_x membrane and Si wafer).

We further performed $C_p(T)$ scans on the phase-separated samples in Figure 4g. The subsequent scans show reproducible cycling with a much higher T_m and T_c (2nd and 3rd scans) than the first scan in Figure 4d. The temperatures are, in fact, close to that of pure Sb_2Se_3. This indicates that the phase that

21951071, 2026, 8, Downloaded from https://advanced.onlinelibrary.wiley.com/doi/10.1002/adom.202503389, Wiley Online Library on [04/03/2026]. See the Terms and Conditions (https://onlinelibrary.wiley.com/terms-and-conditions) on Wiley Online Library for rules of use; OA articles are governed by the applicable Creative Commons License

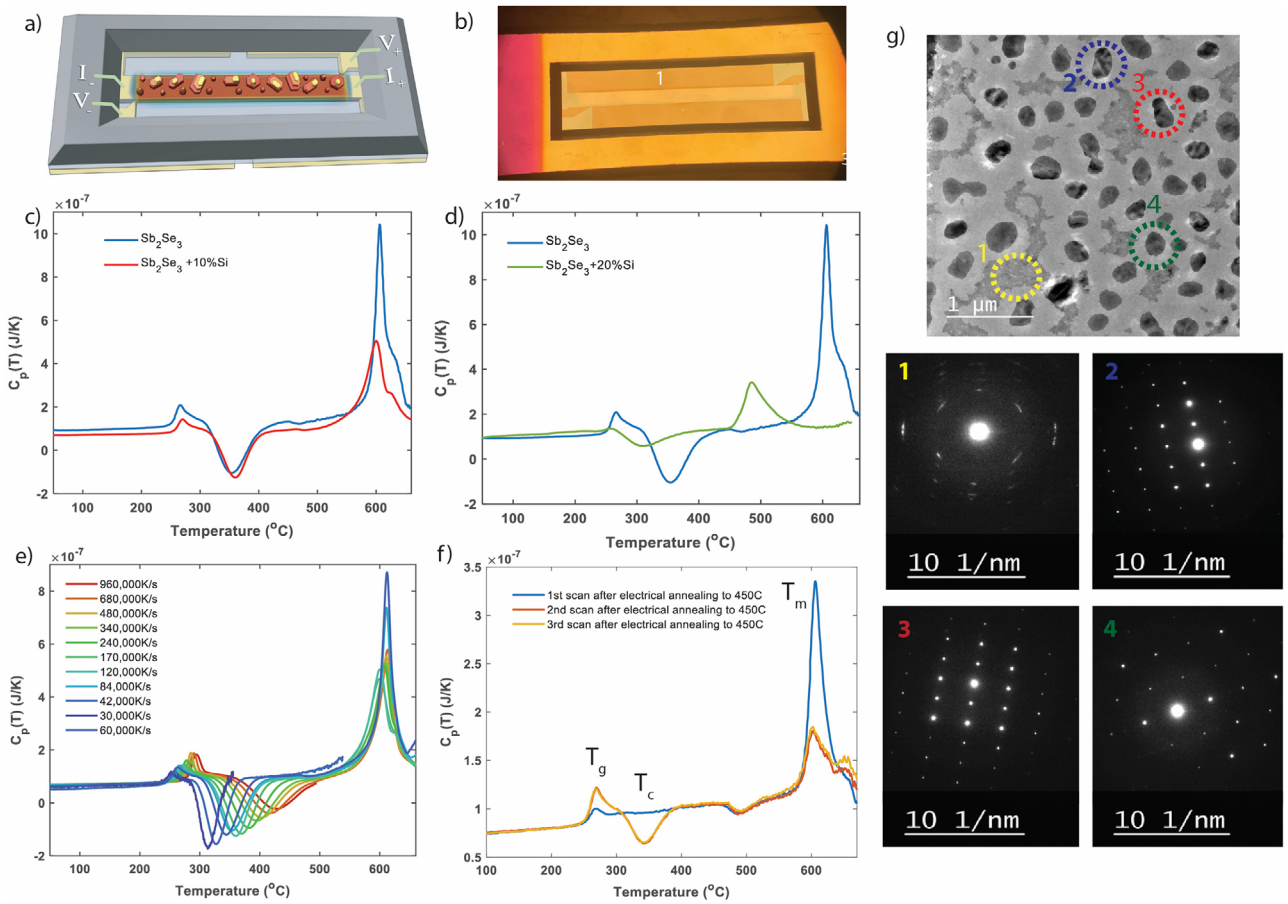

FIGURE 4 | Reversible switching of Si-doped Sb_2Se_3 on NanoDSC. (a) Schematic of the NanoDSC device. (b) Top-view image of NanoDSC. (c) $C_p(T)$ of pre-melted 10%- Si doped sample with a scanning rate of 120,000 K/s. (d) $C_p(T)$ for the first scan of 20%- Si-doped sample. For (c) and (d), $C_p(T)$ of pure Sb_2Se_3 from our other work (unpublished) is included for comparison. (e) and (f) are NanoDSC scans at 120000 K/s of the 10%- Si-doped and 20%- Si-doped samples, respectively. (g) TEM images and selected area diffraction patterns for 20%- Si-doped sample after electrical annealing. The number and color in (g) match the TEM images and selected area electron diffractions.

TABLE 1 | Thermal properties of Si-doped Sb_2Se_3 materials measured through NanoDSC. Activation energy is extracted from a kinetic study (scanning rate dependent). Crystallization temperature is based on data collected at 120000 K/s.

$Si_x(Sb_2Se_3)_{1-x}$	0%	10%	20% (as-deposited scan)	20% (recrystallization scans)
E_a (eV)	1.2	0.9	N/A	1.6
T_c (°C)	351	360	310	345
T_m (°C)	606–610	598–608	484	605

participates in the subsequent melt-quench cycle is Sb_2Se_3 with a low concentration of Si. We note that the glass transition peaks, labeled as T_g in Figure 4f, are more pronounced compared to those in Figure 4e, indicating the existence of an excess amount of glassy phase in the sample. Also, the observation of melting peaks with lower intensities might suggest that only a portion of the material is melting. For the phase-separated 20% Si-doped sample, the cycling portion shows higher activation energy (1.6 eV) compared to pure Sb_2Se_3, as summarized in Table 1. The NanoDSC results suggest, therefore, that the first melting of the as-deposited 20% Si-doped Sb_2Se_3 sample is much lower (490°C) than pure Sb_2Se_3. However, after rapid heating, the sample phase-separated into α (glassy, hard to crystallize, Si-rich) and β (easy to crystallize, Si-poor), forming a nanocomposite. The 20% Si-doped samples were cycled reproducibly for 100 cycles without observable degradation (see Figure S7), indicating that the volume of material undergoing crystallization remains constant throughout cycling and confirming the high reproducibility of the nanocomposite switching behavior. More importantly, NanoDSC revealed that Si dopants slow down the kinetics of phase transition, with the underlying mechanism differing before and after phase segregation. Before phase segregation (the first crystallization event of as-deposited films), the crystallization is dominated by homogeneous nucleation. Si incorporation forms strong tetrahedral Si–Se bonding motifs (supported by Raman spectra), which increase local network rigidity, reduce free

21951071, 2026, 8, Downloaded from https://advanced.onlinelibrary.wiley.com/doi/10.1002/adom.202503389, Wiley Online Library on [04/03/2026]. See the Terms and Conditions (https://onlinelibrary.wiley.com/terms-and-conditions) on Wiley Online Library for rules of use; OA articles are governed by the applicable Creative Commons License

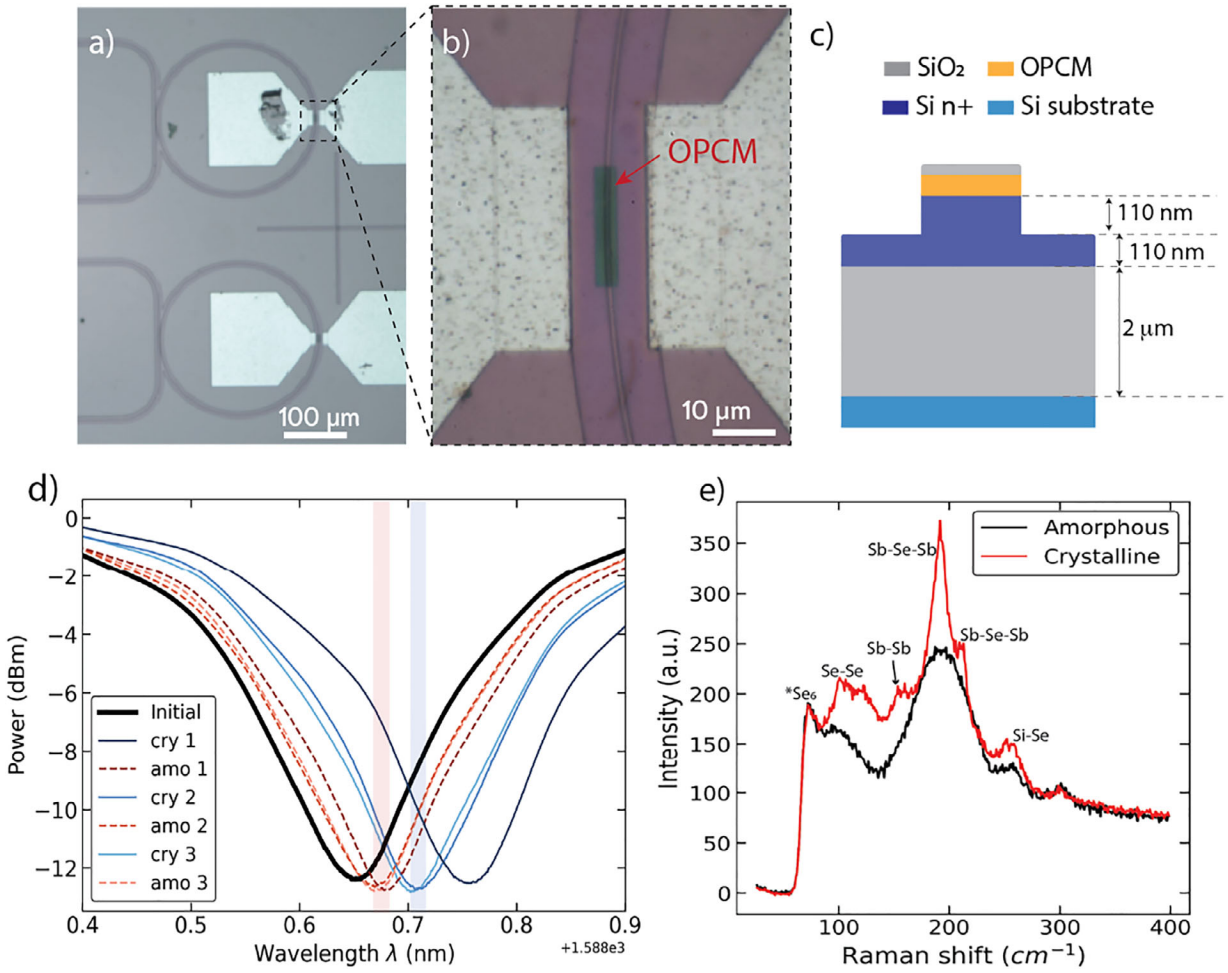

FIGURE 5 | Reversible switching of Si-doped Sb_2Se_3 on PIC. (a) Top-view image of micro-ring resonators with integrated doped-silicon microheaters. (b) Zoom-in image (a), silver regions are contacts of microheaters, and the green region is the OPCM. (c) Cross-section structure of waveguides. (d) Resonance shifts around ~1588 nm. The solid lines represent the transmission measured after applying crystallization pulses, while the dashed lines represent transmissions after amorphization pulses. The highlighted regions in red and blue represent the final stable crystalline and amorphous states, respectively. The numbers represent the cycling order. (e) Raman spectroscopy was measured on the device after the first cycle, i.e., the first re-amorphization and re-crystallization state.

volume, and introduce valence-driven structural frustration. These effects elevate the activation energy for atomic rearrangement and suppress atomic mobility in the initially homogeneous amorphous phase [55]. After phase segregation and during the subsequent recrystallization cycles, rigid Si-rich glassy domains and the reduced percolation connectivity of the Sb_2Se_3 phase further limit long-range diffusion and introduce interfacial diffusion barriers to grain growth—consistent with the elevated activation energies summarized in Table 1.

3 | Device Integration

We now demonstrate that Si- and $SiSe_2$-doped Sb_2Se_3 can be reversibly switched using microheaters for integrated and free-space optical applications—a fundamental test that every OPCM should pass. Even when forming nanocomposites, Sb_2Se_3 is actively switching while Si and $SiSe_2$ form stable amorphous domains, resulting in tunable effective medium optical properties, as shown in Figure S8.

3.1 | Reversible Switching in Photonic Integrated Circuits

To further investigate the thermal and optical properties of Si-doped Sb_2Se_3, we integrated 20% Si-doped Sb_2Se_3 into ring resonators on a silicon-on-insulator platform and performed electro-thermally driven reversible switching. Figure 5a displays the device layout on a partially foundry-fabricated chip [56]. Silicon serves both as the waveguide and as a resistive heater in regions with n^+ doping, enabling the switching of OPCMs through indirect resistive heating, as shown in Figure 5b,c. Figures S9 and S10 show an SEM image and the EDS compositional mapping of the device, respectively. We applied a long, low-power pulse for crystallization and a short, high-power pulse for amorphization, as summarized in Table 2. A 3 V/50 μs pulse is sufficient to crystallize pure Sb_2Se_3; however, surprisingly, only 1.85 V is required to achieve crystallization in the 20% of Si-doped sample. Yet, this 30 ms pulse is significantly longer than the undoped counterparts, which suggests slower kinetics in crystallization. While a 7V/ 500ns pulse is needed for amorphization in

21951071, 2026, 8, Downloaded from https://advanced.onlinelibrary.wiley.com/doi/10.1002/adom.202503389, Wiley Online Library on [04/03/2026]. See the Terms and Conditions (https://onlinelibrary.wiley.com/terms-and-conditions) on Wiley Online Library for rules of use; OA articles are governed by the applicable Creative Commons License

TABLE 2 | Parameters used for on-chip switching of 12-μm long OPCM on PIC.

$Si_x (Sb_2Se_3)_{1-x}$	Voltage (V)	Width (μs)	Power (mW)	Energy (μJ)
x = 0% cry	3.00	50	25.00	2.25
x = 0% amo	7.00	0.5	245.00	0.12
$\Delta n_{eff} = 0.08, \Delta\varphi = \pi$				
x = 20% cry	1.85	3×10^2	23.00	6984.00
x = 20% amo	4.70	1	149.00	0.15
$\Delta n_{eff} = 0.02, \Delta\varphi = 0.2\pi$				

pure Sb_2Se_3, a 4.7V/ 1μs pulse is sufficient to re-amorphize 20% Si-doped sample. Thus, ~150 mW is required to amorphize Si-doped Sb_2Se_3, compared to ~250 mW for pure Sb_2Se_3, as calculated from Joule heating ($P = V^2/R$) [57]. Although a pulse with double duration was required. The evidence of reduced switching power is aligned with the lower T_m observed for the first switching cycle in the temperature-dependent XRD and the first scan on NanoDSC shown above. We note that identical crystallization and amorphization pulses were employed before and after phase segregation. Although the longer pulses reflect slower kinetics introduced by Si dopants, the increased density of nanocrystalline domains and the associated grain boundaries formed after phase segregation could potentially facilitate heterogeneous nucleation and potentially accelerate switching kinetics in later cycles. Yet, the system is complicated, as nanocomposites can act as thermal barriers [58], while the distribution of grain boundaries significantly influences the switching behavior [59]. To identify whether the system is diffusion-limited or nucleation-dominated, as in pure Sb_2Se_3, further detailed kinetic studies are necessary. Moreover, we observed changes in thermal properties across different crystallization regimes (initial crystallization vs. recrystallization after phase segregation). The observed kinetics in our material may limit suitability for high-speed modulation or bit-rate-intensive memory operations. However, many reconfigurable photonic and optical computing applications (e.g., programmable wavelength filters or color pixels, sporadic reconfiguration of PICs, and more) do not require continuous high-rate switching; instead, they benefit from low-loss, nonvolatile state retention. The observed power–time tradeoff reflects intrinsic materials physics rather than device-level optimization.

Using the parameters listed in Table 2, we successfully switched the devices for three cycles, after which the samples were used to perform imaging and characterization in intermediate states. The refractive index contrast in OPCM modulates the effective index of the ring, resulting in a phase shift and thus a change in the device's resonance wavelengths, which we track experimentally, as shown in Figure 5d. We were unable to replicate the amount of redshift during recrystallization and the blueshift in re-amorphization observed in the first cycle, which we attribute to phase segregation (i.e., nanocomposite formation) occurring after the first full switching cycle, as discussed in Section 2.5. The total phase shift in 20% Si-doped (0.2π) is smaller than that of undoped Sb_2Se_3 ($\sim\pi$) for a 12 μm long cell, which is expected, given the smaller contrast in n upon reversible switching (see Figure 1b). Moreover, the quality factors of the microring resonators remained essentially unchanged (see Figure S11) before and after phase segregation and subsequent cycles, suggesting negligible excess loss or structural deterioration during cycling. These results also indicate that effects such as scattering play a minor role in the optical response despite wavelength-comparable features in the nanostructure. In addition, NanoDSC results in Section 2.5 showed that the resulting nanocomposites remain stable for at least 100 switching cycles. Lastly, we note that the switching experiments are intended to demonstrate the feasibility of electro-thermal-driven phase segregation (i.e., nanocomposite formation) and reversible phase switching, rather than to maximize endurance or to establish optimized switching conditions.

By tracking the resonant wavelength shift (λ_{res}), we calculated the refractive index contrast of the material on the PIC (Δn_{eff}) using:

$$\Delta n_{eff} = \frac{\lambda_{res} \times \Delta\varphi}{2\pi \times L}$$

where $\Delta\varphi$ denotes phase shift and is given by $\Delta\varphi = \frac{2\pi \times \Delta\lambda_{res}}{FSR}$, λ_{res} represents the resonance wavelength, FSR is the free spectral range, and L points to the length of the OPCM [60]. As a result, we obtain $\Delta n_{eff} = 0.02$ from the Si-doped device, while $\Delta n_{eff} = 0.08$ is observed in pure Sb_2Se_3. Given that we have identified the refractive index at 1588 nm for the as-deposited film as 2.7, the refractive index for crystalline films can be estimated from the measured value of Δn_{eff}, 0.02. To do this, we performed Finite Element Method simulations using Lumerical Mode, and we found an index of 2.85 for crystalline material, which aligns with the results shown in Figure 1d. The mapping of the Δn_{eff} and sweeping of the refractive index to find the correct experimental value is shown in Figure S12. We note that the impact of reduced Δn on modulation efficiency can be mitigated by increasing the active PCM interaction length, which is feasible given the OPCM's low loss.

Lastly, the Raman spectrum in Figure 5e shows the results for crystallized and then re-amorphized material, displaying Si-Se crystalline resonance bonds, which suggests a potential second phase featuring Si-Se bonds always exists, most likely in the form of $SiSe_2$, which is stable an ambient conditions.

3.2 | $SiSe_2$–Sb_2Se_3 Nanocomposite on Microheaters

Motivated by the results obtained from NanoDSC and DFT calculations, a plausible composition after phase separation is having $SiSe_2$ and Sb_2Se_3, the most thermally stable compounds

21951071, 2026, 8, Downloaded from https://advanced.onlinelibrary.wiley.com/doi/10.1002/adom.202503389, Wiley Online Library on [04/03/2026]. See the Terms and Conditions (https://onlinelibrary.wiley.com/terms-and-conditions) on Wiley Online Library for rules of use; OA articles are governed by the applicable Creative Commons License

in the ternary diagram (see Figure 2a). With this in mind, we describe in Section S13 the co-sputtering of $(SiSe_2)_{0.8}(Sb_2Se_3)_{0.2}$ thin films—a variation from the Si-doped Sb_2Se_3 central to this work—on Ti/Pt microheaters. We successfully switched the materials with consistent pulses (2.5 V/ 1 s for crystallization and 4 V/ 10 µs for amorphization) for 10 cycles, with the corresponding optical contrast seen in Figure S13 $SiSe_2$ has strong covalent bonds, with T_g and T_c of 460°C and 610°C, respectively [61], which are close to the T_m of pure Sb_2Se_3. Therefore, under the same switching conditions used for pure Sb_2Se_3, the $SiSe_2$ phase likely remains amorphous and serves as a stable glassy matrix. At the same time, only the Sb_2Se_3 nanocrystals undergo reversible phase transitions, thus forming an optical phase change nanocomposite. Notably, unlike phase segregation in the Si-doped system, in directly co-sputtered $SiSe_2$–Sb_2Se_3 films, Si is incorporated exclusively as stable $SiSe_2$ structural units from the outset, without forced substitution or aliovalent defects, resulting in chemically abrupt interfaces and a substantially lower defect density. Therefore, although both systems ultimately converge toward the same equilibrium phases, their interfacial bonding, defect landscapes, and switching physics are fundamentally different. To avoid ambiguity arising from the different stoichiometry of the segregated phases after first melt–quench processing, and to keep this work mainly focused on Si-doped Sb_2Se_3, the co-sputtered $(SiSe_2)_{0\cdot8}(Sb_2Se_3)_{0\cdot2}$ device experiments are presented in the Supporting Information for completeness. The device-level switching results of the co-sputtered $(SiSe_2)_{0\cdot8}(Sb_2Se_3)_{0\cdot2}$ films provide two important insights: they enable direct optical reflectance measurements on an electrically driven large-area microheater platform and demonstrate that co-sputtering allows mixing of two potentially immiscible compounds without detectable intermetallic phase formation, while maintaining selective and reversible switching of the Sb_2Se_3 phase. These results support the feasibility of phase-change nanocomposite design through materials phase engineering, using the effective medium theory strategy described in Figure S8.

4 | Conclusions

We studied the effects of Si doping into Sb_2Se_3 using several thin film characterization techniques and reconfigurable devices. We found that after the first melt-quenching process, the initially uniform film undergoes phase segregation, forming a nanocomposite consisting of crystalline Sb_2Se_3 grains embedded in an amorphous $SiSe_2$ matrix. This behavior differs from that of other conventional phase change materials, which typically form multiple crystalline phases [62, 63]. For example, $Ge_4Sb_6Te_7$ forms a coherent nanocomposite with FCC-GeSbTe and SbTe coexisting regions [64–66], which is found to play a significant role in boosting the overall performance of electrical switching. We exploit this phase segregation, which, contrary to being detrimental, allows for the formation of nanocomposites with effective-medium optical properties [67], where the overall optical response arises from the combination of the amorphous matrix and switchable phase-change grains. Our experimental results demonstrate this novel paradigm by achieving a reduction in Sb_2Se_3 optical loss in the visible spectrum with increasing Si doping concentration, albeit at the expense of diminishing the refractive index contrast between states. Moreover, using optimal electrical pulses, we demonstrated the reconfiguration over a few cycles of Si-incorporated Sb_2Se_3 embedded into photonic integrated circuits. Thus, demonstrating that even after phase segregation, the phase-changing nature of Sb_2Se_3 allows for optical reconfiguration while the amorphous matrix remains essentially unchanged and contributes to the effective medium response. While Si-doped Sb_2Se_3 served as a platform to demonstrate and understand OPCM nanocomposites, this particular system is promising and could be further engineered to display optimal properties tailored for specific applications.

Doping also impacts thermal behavior. Using a novel NanoDSC technique, we uncovered that the Si dopant suppresses crystallization by slowing the kinetics of phase transition, which can be understood by considering two regimes: before and after phase segregation. Complementary PIC measurements further reveal thermal changes by examining the relationship between applied switching pulses and the evolution of resonance shift in microring resonators during phase transitions. However, due to the technical challenges of probing nanometer-sized grains and isolating Si% in a Si-rich multi-layered device structure, we could not conclude the exact chemical stoichiometry of the nanocomposite components after phase segregation. Future research using TEM–EELS could enable quantitative subwavelength compositional mapping to fully validate the nanocomposite model.

Our results demonstrate a materials-design strategy that leverages nanocomposites formed by phase segregation to achieve an optimized combination of functional properties while preserving the reversible switching of OPCMs. This work, however, represents the first instance of such an approach and could benefit from further studies. Namely, understanding phase segregation for different thicknesses, which can introduce thermal inhomogeneity and modify the effective quench/crystallization conditions [43], and degradation mechanisms such as thermally induced mechanical stress, interfacial delamination, film dewetting, and further elemental redistribution [68], which may contribute to the failure of photonic devices. Nanocomposites can enable engineered optical and thermal properties, which are pivotal for OPCMs; thus, opening a path for future OPCM engineering and enabling tailored properties for applications in nonvolatile optical memories, modulators, metasurfaces, and more.

5 | Experimental Section

5.1 | Thin-Film Synthesis

We deposited binary thin film composition spreads on 400 µm-thick sapphire substrates using an ultrahigh vacuum (base pressure: 2×10^{-8} Torr) magnetron sputtering system (AJA Orion-3) at room temperature. We used two approaches for the spread: a continuous and a patterned gradient, as shown in Figures S1 and S2. The latter employed a silicon mask placed in contact with the substrate to delineate 15 individual compositions evenly with a 4.5 mm separation. High purity Si (99.995%) and Sb_2Se_3 (99.999%) targets (Kurt J. Lesker Co.) used to co-sputter in ultrahigh purity Argon (99.9997%, Airgas) at a pressure of 4.6×10^{-3} Torr. The thin film spread was deposited over 25 min using 14W and 17W RF power sources for Si and Sb_2Se_3, respectively. The co-sputtering results in an intrinsic continuous thickness gradient

21951071, 2026, 8, Downloaded from https://advanced.onlinelibrary.wiley.com/doi/10.1002/adom.202503389, Wiley Online Library on [04/03/2026]. See the Terms and Conditions (https://onlinelibrary.wiley.com/terms-and-conditions) on Wiley Online Library for rules of use; OA articles are governed by the applicable Creative Commons License

(120–30 nm). The thin films were capped with 30 nm SiO_2 to avoid surface contamination and, in some cases, with 5 nm Au/Pd to avoid charging under electron microscopy (except TEM). To prepare crystalline samples, the thin film spreads were annealed on a hotplate in an N_2 glove box for 20 mins at temperatures ranging from 200°C to 350°C. Note that some samples were annealed longer to compare the phase transition kinetics across compositions. Thin film deposition on PIC and NanoDSC sensors was carried out by placing devices at the position where the targeted composition was achieved.

5.2 | Device Fabrication and Measurement Methods

The PIC devices were fabricated on 220-nm silicon-on-insulator (SOI) wafers, following the fabrication process described by Rios et al. [56]. We used micro-ring resonators with embedded n^{++}-dope microheaters. A 30-nm-thick PCM and 10-nm-thick SiO_2 were deposited via sputtering, described in Section 4.1. Electron beam lithography (Elionix ELS-G100 system) was used to pattern the photonic circuitry, followed by CF_4 reactive ion etching (Trion RIE). The transmission spectrum measurements and hardware for on-chip electrical switching followed the process thoroughly described in Sun et al. [3].

Thin-film samples were deposited onto the NanoDSC sensors for calorimetric measurement. The sensors were fabricated at the Cornell Nanoscale Facility using standard microelectromechanical systems (MEMS) fabrication methods [69]. A 50 nm Pt film, which performs as the heater and thermometer in the calorimetric cell, was sputtered on the low-stress free-standing SiN_x (100 nm) membrane. The membrane was supported by a 500 μm-thick silicon frame. The back side of each sensor was patterned with four Pt electrodes (V+, V-, I+, I-) for four-point resistance measurements. Empty sensors were annealed in vacuum (2×10^{-7} Torr) to minimize resistance drift (<1% per 1,000 pulses to 750°C). Thin-film samples were deposited on the front side of the sensor using a self-aligned shadow mask to ensure alignment between the sample and calorimetric sensing region (0.5 mm × 5 mm). More details on the design and fabrication of the NanoDSC sensors were described in Ref [70]. Differential mode NanoDSC measurements were performed in vacuum (2×10^{-7} Torr) by applying synchronized direct-current pulses (duration 1–25 ms) to both sample and reference sensors. For each scan, the Joule heating leads to rapid temperature ramping of the sample from room temperature to a maximum temperature in the 100–720°C range with a controlled heating rate ranging from 8×10^3 to 1×10^6 K/s, followed by a passive cooling down ($\sim 1 \times 10^4$ K/s) back to room temperature. The sample heat capacity $C_p(T)$ during the heating cycle was calculated based on the voltage difference between the two sensors with necessary baseline corrections, including heat loss and the difference between the sample/reference addenda. NanoDSC data analysis in differential mode was detailed in our previous work [54, 63].

Sb_2Se_3 and $SiSe_2$ (target with 99.5% purity from AJA Inc.) thin films were deposited via co-sputtering using 15W and 11W RF power at 4.6×10^{-3} Torr. The microheaters were fabricated with 10 nm- Ti and 50nm- Pt buried in a trench made by thermal oxide, etched by fluorine etcher (Oxford Plasmalab System 100). The bowtie microheaters consist of 100 x100 μm^2 metal contacts and 12x14 μm^2 bridge, covered with 30-nm- thick $Sb_2Se_3/SiSe_2$ thin-films. The metals were evaporated, followed by lift-off, and $Sb_2Se_3/SiSe_2$ was etched with CF_4 reactive ion etching (Trion RIE). All the patterning was done by photolithography (Maskless Aligner, Heidelberg). The electrical switching followed the process as that used on the PIC platform.

5.3 | Characterization Methods

Chemical composition of Si-Sb-Se thin film library determined by using wavelength dispersive spectroscopy (WDS) in an electron probe microanalyzer (JXA 8900R Microprobe), with an acceleration voltage of 15 kV. Calibration was done using polished pure metal with an experimental error margin of <0.3 at. %. To capture morphologies and qualitative chemical composition on the device, a Tescan GAIA system was used for scanning electron microscopy (SEM) and energy dispersive spectroscopy (EDS) with 10 kV acceleration voltage.

Ellipsometry was performed using a Woollam Variable Angle Spectroscopic Ellipsometry (VASE) system to collect and analyze the optical properties in the 245–1689 nm spectrum, at 55°, 60°, and 65° angles of incidence. The dielectric response fitting was based on Tauc-Lorentz dispersion oscillators, and mean squared error (MSE) was used as an index for fitting.

The thin film spread was cut into smaller pieces with the desired compositional range. A Discover powder diffractometer (Bruker C2/D8) of CuKα radiation with a high-temperature stage was used to collect X-ray diffraction (XRD) images. The exposure time was 5 min for each frame. The diffraction was integrated into 1D data with the 2θ range from 14° to 60°. To avoid oxidation, the stage was covered by a graphite dome under vacuum (~ 5 Torr). Temperature-dependent XRD was conducted from room temperature (30°C) to temperatures over T_m (800°C) in discrete steps of 50°C or 100°C. The temperature ramp rate was 20°C/ min with a 5 min hold time to reach equilibrium.

The OPCM phase analysis was performed using surface-enhanced Raman spectroscopy (Yvon Jobin LabRam ARAMIS) with a 532 nm laser, a 2400 lines/mm grating, and a 100 × long-working-distance objective lens.

The 100 nm SiN_x membrane of the NanoDSC sensor makes it possible to conduct direct TEM characterization on the post-scanned thin-film sample using a home-built holder. In this study, sample morphology after NanoDSC scans was obtained using a JEOL 2100 TEM at 200 kV acceleration voltage. The local structure was studied using selected area diffraction with a camera length of 25 cm.

Optical measurements were conducted by directly capturing the intensity of light reflected from the surface of the fabricated device, which was mounted on a motorized XYZ-translation stage. A visible-range LED source (HLV3-24SW) was focused onto the device using a Navita coaxial vision system with up to 30 × magnification. To simultaneously visualize the device and acquire the reflected signal, a beam splitter was employed to

21951071, 2026, 8, Downloaded from https://advanced.onlinelibrary.wiley.com/doi/10.1002/adom.202503389, Wiley Online Library on [04/03/2026]. See the Terms and Conditions (https://onlinelibrary.wiley.com/terms-and-conditions) on Wiley Online Library for rules of use; OA articles are governed by the applicable Creative Commons License

evenly direct the light to both a CCD camera (Amscope MU500-HS) for imaging and a Horiba spectrometer (Horiba iHR-320) for reflection spectrum acquisition. The measured reflection spectra were normalized by dividing the collected signal by the intensity of a reference beam reflected from a smooth Ti (10 nm)/Pt (90 nm) surface with the same illumination spot size.

5.4 | Computational Methods

The density functional theory (DFT) calculations were conducted using the Vienna Ab initio Simulation Package (VASP) [71] with the Perdew–Burke–Ernzerhof exchange-correlation functional [72]. Our supercell model of Si-doped Sb_2Se_3 follows previous computational studies of the Ge – Sb – Te system [73]; as a substitutional cation dopant, Si would occupy Sb sites and introduce vacancies into the cation sublattice. Raman spectroscopy results suggest the presence of Si – Se bonds supporting this assumption (see Results section for details). Taking Si to have its standard 4+ oxidation state, we used the following defect reaction was used:

$$3SiSe_2 \underset{Sb_2Se_3}{\rightarrow} 3Si_{Sb}^{\circ} + V_{Sb}^{'''} + 6Se_{Se}$$

We created 4 supercells of orthorhombic Sb_2Se_3 with increasing Si concentrations: 0% Si (0 Si, 24 Sb, 36 Se), 5.1% Si (3 Si, 20 Sb, 36 Se), 10.3% Si (6 Si, 16 Sb, 36 Se), and 15.8% Si, (9 Si, 12 Sb, 36 Se). To determine the optimal arrangement of Si atoms and Sb vacancies, we used pymatgen [74] to enumerate every possible arrangement of Si atoms and vacancies in each supercell. Then, the 10 structures with the lowest Ewald energy [75] were relaxed with DFT. The structures with the lowest DFT energy were selected as the representative structures for subsequent bandgap calculations. The bandgap calculations were performed using the parameters generated by pymatgen [74] as in the Materials Project [76].

The simulations of the silicon waveguide modes for the different phase states of Si-Sb_2Se_3 were performed using Lumerical MODE (Ansys).

Acknowledgements

C.R.O., J.H., N.Y, and I.T. acknowledge funding provided by the National Science Foundation (awards ECCS-2210168/2210169, ECCS-2430920, and DMR-2329087/2329088), supported in part by industry partners, as specified in the Future of Semiconductors (FuSe) program. J.Z. and L.H.A. acknowledge the financial support by NSF-DMR-1409953 and NSF-DMR-1809573. The NanoDSC sensors were fabricated at the Cornell Nanoscale Facility (project #522-94), a member of the National Nanotechnology Infrastructure Network (NNIN). Materials characterization was conducted in part at the Materials Research Laboratory, University of Illinois, and the NanoCenter, University of Maryland.

Conflicts of Interest

The authors declare no conflicts of interest.

Data Availability Statement

The data that support the findings of this study are available from the corresponding author upon reasonable request.

References

1. C. Ríos, M. Stegmaier, P. Hosseini, et al., "Integrated All-Photonic Non-Volatile Multi-Level Memory," *Nature Photonics* 9 (2015): 725–732.

2. G. Wang, J. Shen, Y. He, et al., "Programmable Non-Volatile Photonic Analog-to-Digital Converter Based on Back-End-of-Line Compatible Phase-Change Materials," *Advanced Materials* 37 (2025): 2419444.

3. H. Sun, C. Lian, F. Vásquez-Aza, et al., "Microheater Hotspot Engineering For Spatially Resolved And Repeatable Multi-Level Switching In Foundry-Processed Phase Change Silicon Photonics," *Nature Communications* 16 (2025): 4291.

4. Y.-S. Huang, C.-Y. Lee, M. Rath, et al., "Tunable Structural Transmissive Color In Fano-Resonant Optical Coatings Employing Phase-Change Materials," *Materials Today Advances* 18 (2023): 100364.

5. S. Abdollahramezani, O. Hemmatyar, M. Taghinejad, et al., "Electrically Driven Reprogrammable Phase-Change Metasurface Reaching 80% Efficiency," *Nature Communications* 13 (2022): 1696.

6. Q. Wang, E. T. F. Rogers, B. Gholipour, et al., "Optically Reconfigurable Metasurfaces And Photonic Devices Based On Phase Change Materials," *Nature Photonics* 10 (2016): 60–65.

7. Y. Zhang, C. Fowler, J. Liang, et al., "Electrically Reconfigurable Non-Volatile Metasurface Using Low-Loss Optical Phase-Change Material," *Nature Nanotechnology* 16 (2021): 661–666.

8. K. Chaudhary, M. Tamagnone, X. Yin, et al., "Polariton Nanophotonics Using Phase-Change Materials," *Nature Communications* 10 (2019): 4487.

9. Y.-S. Huang, C.-Y. Lee, I. Takeuchi, and C. A. R. Ocampo, "Optical Phase Change Materials," *Annual Review of Materials Research* 55 (2025): 255–283.

10. P. Prabhathan, K. V. Sreekanth, J. Teng, et al., "Roadmap For Phase Change Materials In Photonics And Beyond," *iScience* 26 (2023): 107946.

11. A. Albanese, M. Tomelleri, L. Karam, et al., "Optical Properties of $GeSe_{1-x}Te_x$ Chalcogenide Materials Promising for on-Chip Low and Ultra-Low Loss Reconfigurable Photonics and Nonlinear Devices," *physica status solidi (RRL)–Rapid Research Letters* 18 (2024): 2400129.

12. Y. Zhang, J. B. Chou, J. Li, et al., "Broadband Transparent Optical Phase Change Materials For High-Performance Nonvolatile Photonics," *Nature Communications* 10 (2019): 4279.

13. A. Shongalova, M. R. Correia, J. P. Teixeira, et al., "Growth of Sb_2Se_3 Thin Films By Selenization of RF Sputtered Binary Precursors," *Solar Energy Materials and Solar Cells* 187 (2018): 219–226.

14. T. Zhai, M. Ye, L. Li, et al., "Single-Crystalline Sb_2Se_3 Nanowires for High-Performance Field Emitters and Photodetectors," *Advanced Materials* 22 (2010): 4530–4533.

15. M. Delaney, I. Zeimpekis, D. Lawson, D. W. Hewak, and O. L. Muskens, "A New Family of Ultralow Loss Reversible Phase-Change Materials for Photonic Integrated Circuits: Sb_2S_3 and Sb_2Se_3," *Advanced Functional Materials* 30 (2020): 2002447.

16. M. S. Arjunan, S. Durai, A. Mondal, K. N. V. D. Adarsh, and A. Manivannan, "Realization of 4-Bit Multilevel Optical Switching in $Ge_2Sb_2Te_5$ and $Ag_5In_5Sb_{60}Te_{30}$ Phase-Change Materials Enabled in the Visible Region," *ACS Applied Electronic Materials* 2 (2020): 3977–3986.

17. N. A. Nobile, C. Lian, H. Sun, et al., "Nonvolatile Tuning Of Bragg Structures Using Transparent Phase-Change Materials," *Optical Materials Express* 13 (2023): 2700–2710.

18. R. C. Devlin, M. Khorasaninejad, W. T. Chen, J. Oh, and F. Capasso, "Broadband High-Efficiency Dielectric Metasurfaces For The Visible Spectrum," *Proceedings of the National Academy of Sciences* 113 (2016): 10473–10478.

19. A. Katiyi and A. Karabchevsky, "Quantum Photonics On A Chip," *APL Quantum* 2 (2025): 020901.

21951071, 2026, 8, Downloaded from https://advanced.onlinelibrary.wiley.com/doi/10.1002/adom.202503389, Wiley Online Library on [04/03/2026]. See the Terms and Conditions (https://onlinelibrary.wiley.com/terms-and-conditions) on Wiley Online Library for rules of use; OA articles are governed by the applicable Creative Commons License

20. N. Youngblood, C. Talagrand, B. F. Porter, et al., "Reconfigurable Low-Emissivity Optical Coating Using Ultrathin Phase Change Materials," *ACS Photonics* 9 (2022): 90–100.

21. L. Guarneri, S. Jakobs, A. von Hoegen, et al., "Metavalent Bonding in Crystalline Solids: How Does It Collapse?," *Advanced Materials* 33 (2021): 2102356.

22. S. Wintersteller, O. Yarema, D. Kumaar, et al., "Unravelling The Amorphous Structure And Crystallization Mechanism of GeTe Phase Change Memory Materials," *Nature Communications* 15 (2024): 1011.

23. Y. Lai, B. Qiao, J. Feng, et al., "Nitrogen-Doped $Ge_2Sb_2Te_5$ Films For Nonvolatile Memory," *Journal of Electronic Materials* 34 (2005): 176–181.

24. A. Ebina, M. Hirasaka, and K. Nakatani, "Oxygen Doping Effect On Ge–Sb–Te Phase Change Optical Disks," *Journal of Vacuum Science & Technology A: Vacuum, Surfaces, and Films* 17 (1999): 3463–3466.

25. X. Zhou, M. Xia, F. Rao, et al., "Understanding Phase-Change Behaviors of Carbon-Doped $Ge_2Sb_2Te_5$ for Phase-Change Memory Application," *ACS Applied Materials & Interfaces* 6 (2014): 14207–14214.

26. X. Chen, Y. Zheng, M. Zhu, et al., "Scandium Doping Brings Speed Improvement In Sb_2Te Alloy For Phase Change Random Access Memory Application," *Scientific Reports* 8 (2018): 6839.

27. A. A. E. Adam, X. Cheng, H. H. Abuelhassan, and X. S. Miao, "Microstructure and Magnetic Behavior of Mn doped GeTe Chalcogenide Semiconductors Based Phase Change Materials," *Solid State Communications* 259 (2017): 19–23.

28. Q. Wang, P. M. Konze, G. Liu, et al., "Transition Metal Doping of Phase Change Materials: Atomic Arrangement of Cr-Doped $Ge_2Sb_2Te_5$," *The Journal of Physical Chemistry C* 123 (2019): 30640–30648.

29. Y. Hu, X. Zhu, H. Zou, L. Zheng, S. Song, and Z. Song, "O-Doped Sb Materials For Improved Thermal Stability And High-Speed Phase Change Memory Application," *Journal of Alloys and Compounds* 696 (2017): 150–154.

30. C. Fan, Z. Gu, J.-Q. Wang, X. Shen, and Y. Chen, "Crystallization Kinetics of Sb Nanocomposite Phase-Change Materials with Strong Oxide Doping," *Ceramics International* 51 (2025): 30341–30347.

31. K. Peng, Y. Chen, W. Leng, et al., "Tailorable Fragile-To-Strong Kinetics Features Of Metal Oxides Nanocomposite Phase-Change Antimony Films," *Acta Materialia* 234 (2022): 118013.

32. Z. Wang, S. Bae, M. Baljozović, et al., "One-Step Hydrothermal Synthesis of Sn-Doped Sb_2Se_3 for Solar Hydrogen Production," *ACS Catalysis* 14 (2024): 9877–9886.

33. G. Spaggiari, D. Bersani, D. Calestani, et al., "Exploring Cu-Doping for Performance Improvement in Sb_2Se_3 Photovoltaic Solar Cells," *International Journal of Molecular Sciences* 23 (2022): 15529.

34. Y. Hu, H. Zou, L. Yuan, et al., "Improved Phase Change Behavior Of Sb_2Se Material By Si Addition For Phase Change Memory," *Scripta Materialia* 115 (2016): 19–23.

35. Q. Liu, T. Wei, Y. Zheng, et al., "Picosecond Operation of Optoelectronic Hybrid Phase Change Memory Based on Si-Doped Sb Films," *Advanced Functional Materials* 35 (2025): 2417128.

36. K. Lei, M. Wei, Z. Chen, et al., "Magnetron-Sputtered And Thermal-Evaporated Low-Loss Sb-Se Phase-Change Films In Non-Volatile Integrated Photonics," *Optical Materials Express* 12 (2022): 2815–2823.

37. T. Y. Teo, M. Krbal, J. Mistrik, J. Prikryl, L. Lu, and R. E. Simpson, "Comparison And Analysis Of Phase Change Materials-Based Reconfigurable Silicon Photonic Directional Couplers," *Optical Materials Express* 12 (2022): 606–621.

38. K. V. Shportko, "Disorder And Compositional Dependences in Urbach-Martienssen Tails In Amorphous $(GeTe)_x(Sb_2Te_3)_{1-x}$ Alloys," *Scientific Reports* 9 (2019): 6030.

39. Y. Fu and M. Willander, *Physical Models of Semiconductor Quantum Devices*, (Eds.: Y. Fu, M. Willande), (Springer, 1999): 75–102, https://www.google.com/books/edition/Physical_Models_of_Semiconductor_Quantum/1TfesqF88T0C?hl=en.

40. H. Ticha and L. Tichy, "Remark On The Correlation Between The Refractive Index And The Optical Band Gap In Some Crystalline Solids," *Materials Chemistry and Physics* 293 (2023): 126949.

41. F. Naccarato, F. Ricci, J. Suntivich, G. Hautier, L. Wirtz, and G.-M. Rignanese, "Searching For Materials With High Refractive Index And Wide Band Gap: A First-Principles High-Throughput Study," *Physical Review Materials* 3 (2019): 044602.

42. J. P. Perdew and M. Levy, "Physical Content of the Exact Kohn-Sham Orbital Energies: Band Gaps and Derivative Discontinuities," *Physical Review Letters* 51 (1983): 1884.

43. D. Lawson, S. Blundell, M. Ebert, O. L. Muskens, and I. Zeimpekis, "Optical Switching Beyond A Million Cycles Of Low-Loss Phase Change Material Sb_2Se_3," *Optical Materials Express* 14 (2024): 22–38.

44. A. Kumar, V. Kumar, A. Romeo, C. Wiemer, and G. Mariotto, "Raman Spectroscopy and In Situ XRD Probing of the Thermal Decomposition of Sb_2Se_3 Thin Films," *The Journal of Physical Chemistry C* 125 (2021): 19858–19865.

45. S. Guo, Y. Wang, X. Zhang, B. Wang, and Z. Hu, "Phase Change Behavior Improvement of Sb_2Te_3 Films By Si Doping: Raman Scattering Evidence At Elevated Temperatures," *AIP Advances* 12 (2022): 035002.

46. R. Hunger, N. Blick, N. Esser, et al., "Growth of Sb on Si(111) Studied by Raman Scattering," *Surface Science* 307-309 (1994): 1061–1065.

47. X. Wang, K. Kunc, I. Loa, U. Schwarz, and K. Syassen, "Effect Of Pressure On The Raman Modes Of Antimony," *Physical Review B* 74 (2006): 134305.

48. Z. G. Ivanova, E. Cernoskova, V. S. Vassilev, and S. V. Boycheva, "Thermomechanical And Structural Characterization of $GeSe_2$–Sb_2Se_3–ZnSe Glasses," *Materials Letters* 57 (2003): 1025–1028.

49. M. Tenhover, M. A. Hazle, and R. K. Grasselli, "Atomic Structure of SiS_2 and $SiSe_2$ Glasses," *Physical Review Letters* 51 (1983): 404.

50. J. E. Griffiths, M. Malyj, G. P. Espinosa, and J. P. Remeika, "Crystalline $SiSe_2$ and $SixSe_{1-x}$ Glasses: Syntheses, Glass Formation, Structure, Phase Separation, And Raman Spectra," *Physical Review B* 30 (1984): 6978.

51. L. Hu, L. P. De La Rama, M. Y. Efremov, Y. Anahory, F. Schiettekatte, and L. H. Allen, "Synthesis and Characterization of Single-Layer Silver−Decanethiolate Lamellar Crystals," *Journal of the American Chemical Society* 133 (2011): 4367–4376.

52. S. L. Lai, J. Y. Guo, V. Petrova, G. Ramanath, and L. H. Allen, "Size-Dependent Melting Properties of Small Tin Particles: Nanocalorimetric Measurements," *Physical Review Letters* 77 (1996): 99.

53. M. Zhang, M. Y. Efremov, F. Schiettekatte, et al., "Size-Dependent Melting Point Depression Of Nanostructures: Nanocalorimetric Measurements," *Physical Review B* 62 (2000): 10548.

54. J. Zhao, J. Hui, Z. Ye, et al., "Exploring "No Man's Land"—Arrhenius Crystallization of Thin-Film Phase Change Material at 1 000 000 K s −1 via Nanocalorimetry," *Advanced Materials Interfaces* 9 (2022): 2200429.

55. J. C. Phillips, "Topology Of Covalent Non-Crystalline Solids I: Short-Range Order In Chalcogenide Alloys," *Journal of Non-Crystalline Solids* 34 (1979): 153–181.

56. C. Ríos, Q. Du, Y. Zhang, et al., "Ultra-Compact Nonvolatile Phase Shifter Based On Electrically Reprogrammable Transparent Phase Change Materials," *PhotoniX* 3 (2022): 26.

57. Z. Fang, R. Chen, J. Zheng, et al., "Ultra-Low-Energy Programmable Non-Volatile Silicon Photonics Based On Phase-Change Materials With Graphene Heaters," *Nature Nanotechnology* 17 (2022): 842–848.

58. J. Shen, S. Lv, X. Chen, et al., "Thermal Barrier Phase Change Memory," *ACS Applied Materials & Interfaces* 11 (2019): 5336–5343.

21951071, 2026, 8, Downloaded from https://advanced.onlinelibrary.wiley.com/doi/10.1002/adom.202503389, Wiley Online Library on [04/03/2026]. See the Terms and Conditions (https://onlinelibrary.wiley.com/terms-and-conditions) on Wiley Online Library for rules of use; OA articles are governed by the applicable Creative Commons License

59. Y. Xue, S. Song, X. Chen, et al., "Enhanced Performance Of Phase Change Memory By Grain Size Reduction," *Journal of Materials Chemistry C* 10 (2022): 3585–3592.

60. M. A. Mohammed, J. Melskens, R. Stabile, et al., "Metastable Refractive Index Manipulation in Hydrogenated Amorphous Silicon for Reconfigurable Photonics," *Advanced Optical Materials* 8 (2020): 1901680.

61. K. Chandra Mondal, S. Roy, B. Dittrich, et al., "A Soluble Molecular Variant Of The Semiconducting Silicondiselenide," *Chemical Science* 6 (2015): 5230–5234.

62. S. Ran, E. Petroni, L. Laurin, et al., "Phase Transitions And Chemical Segregation in Ge-Rich GST Based Phase Change Memory Cells," *Scientific Reports* (2025) 15: 11357.

63. J. Zhao, A. I. Khan, M. Y. Efremov, et al., "Probing the Melting Transitions in Phase-Change Superlattices via Thin Film Nanocalorimetry," *Nano Letters* 23 (2023): 4587–4594.

64. A. G. Kusne, H. Yu, C. Wu, et al., "On-The-Fly Closed-Loop Materials Discovery Via Bayesian Active Learning," *Nature Communications* 11 (2020): 5966.

65. X. Wu, A. I. Khan, H. Lee, et al., "Novel Nanocomposite-Superlattices For Low Energy And High Stability Nanoscale Phase-Change Memory," *Nature Communications* 15 (2024): 13.

66. A. I. Khan, H. Yu, H. Zhang, et al., "Energy Efficient Neuro-Inspired Phase–Change Memory Based on $Ge_4Sb_6Te_7$ as a Novel Epitaxial Nanocomposite," *Advanced Materials* 35 (2023): 2300107.

67. D. Stroud, "Generalized Effective-Medium Approach To The Conductivity Of An Inhomogeneous Material," *Physical Review B* 12 (1975): 3368.

68. C. C. Popescu, K. Aryana, B. Mills, et al., "Understanding and Circumventing Failure Mechanisms in Chalcogenide Optical Phase Change Material $Ge_2Sb_2Se_4$ Te," *Advanced Optical Materials* 13 (2025): 2402751.

69. D. W. Denlinger, E. N. Abarra, K. Allen, et al., "Thin Film Microcalorimeter For Heat Capacity Measurements From 1.5 to 800 K," *Review of Scientific Instruments* 65 (1994): 946–959.

70. M. Y. Efremov, E. A. Olson, M. Zhang, F. Schiettekatte, Z. Zhang, and L. H. Allen, "Ultrasensitive, Fast, Thin-Film Differential Scanning Calorimeter," *Review of Scientific Instruments* 75 (2004): 179–191.

71. G. Kresse and J. Hafner, "Ab Initio Molecular Dynamics For Liquid Metals," *Physical Review B* 47 (1993): 558.

72. J. P. Perdew, K. Burke, and M. Ernzerhof, "Generalized Gradient Approximation Made Simple," *Physical Review Letters* 77 (1996): 3865.

73. J.-W. Park, S. H. Eom, H. Lee, et al., "Optical Properties Of Pseudobinary GeTe, $Ge_2Sb_2Te_5$, $GeSb_2Te_4$, $GeSb_4Te_7$, and Sb_2Te_3 From Ellipsometry And Density Functional Theory," *Physical Review B* 80 (2009): 115209.

74. S. P. Ong, W. D. Richards, A. Jain, et al., "Python Materials Genomics (Pymatgen): A Robust, Open-Source Python Library For Materials Analysis," *Computational Materials Science* 68 (2013): 314–319.

75. A. Y. Toukmaji and J. A. Board, "Ewald Summation Techniques In Perspective: A Survey," *Computer Physics Communications* 95 (1996): 73–92.

76. A. Jain, G. Hautier, C. J. Moore, et al., "A High-Throughput Infrastructure For Density Functional Theory Calculations," *Computational Materials Science* 50 (2011): 2295–2310.

Supporting Information

Additional supporting information can be found online in the Supporting Information section.

Supporting File: adom71005-sup-0001-SuppMat.pdf.

21951071, 2026, 8, Downloaded from https://advanced.onlinelibrary.wiley.com/doi/10.1002/adom.202503389, Wiley Online Library on [04/03/2026]. See the Terms and Conditions (https://onlinelibrary.wiley.com/terms-and-conditions) on Wiley Online Library for rules of use; OA articles are governed by the applicable Creative Commons License